PAPER

Group-I lead oxide X$_2$PbO$_3$ (X = Li, Na, K, Rb, and Cs) glass-like materials for energy applications: a hybrid-DFT study

R. Zosiamliana,[ab] Lalhriat Zuala,[b] Lalrinthara Pachuau,[b] Lalmuanpuia Vanchhawng,[b] S. Gurung,[b] A. Laref, [c] Shalika R. Bhandari [*d] and D. P. Rai [*a]

Pb-based compounds have garnered considerable theoretical and experimental attention due to their promising potential in energy-related applications. In this study, we explore the glass-like alkali metal lead oxides X$_2$PbO$_3$ (X = Li, Na, K, Rb, Cs) and assess their suitability for piezoelectric and thermoelectric applications. First-principles calculations were performed using hybrid density functional theory (DFT), incorporating B3LYP, HSE06, and PBE0 functionals. Among these, PBE0 is identified as the most accurate, yielding lattice parameters in close agreement with experimental data. Structural stability was confirmed through the evaluation of thermal, mechanical, and formation energies. For the non-centrosymmetric orthorhombic phase *Cmc*2$_1$-X$_2$PbO$_3$ (X = K, Rb, Cs), piezoelectric constants were computed *via* both the numerical Berry phase (BP) method and the analytical Coupled Perturbed Hartree−Fock/Kohn−Sham (CPHF/KS) formalism. Notably, Cs$_2$PbO$_3$ exhibited a piezoelectric coefficient of $e_{33} = 0.60$ C m^{-2} (CPHF/KS), while K$_2$PbO$_3$ showed $e_{32} = -0.51$ C m^{-2} (BP). Thermoelectric properties were investigated using the semiclassical Boltzmann transport theory within the rigid band approximation. The calculated thermoelectric performance reveals promising figures of merit (*ZT*), ranging from 0.3 to 0.63, suggesting these materials are applicable as future thermoelectric materials.

1 Introduction

Energy generation and storage is crucial to meet the current global energy and environmental crises. The energy extracted from fossil fuels is extensively utilized for transportation, many industries and many other purposes, despite its known harmful effect.[1] Thermoelectricity holds promise as a suitable and sustainable alternative to greenhouse gases emitting fuels if efficient thermoelectric (TE) devices of high heat energy-to-electric voltage conversion efficiency can be discovered.[2–6] First-principles calculations with the incorporation of Boltzmann transport equation *via* the BoltzTraP code[7] can help in predicting the candidates for the preparation of TE devices. Glass-like compounds have become fascinating materials, both experimentally and theoretically, due to the complexity of their structures which in turn exhibit low lattice thermal conductivity, tunable electronic properties, and flexibility in

fabrication.[8–11] Although silicate (SiO$_2$) glasses are widely abundant and commonly used materials, they have significant limitations such as brittleness, high resistance and phase transition at higher temperatures, *etc.* Therefore, it is pivotal for researchers to find proper replacements for silicate glasses.[12] In this novel work, we propose alkali metal oxide Pb-based glass-like materials X$_2$PbO$_3$ (X = Li, Na, K, Rb, Cs) as potential replacements for SiO$_2$-glasses such as: Li$_2$SiO$_3$, Na$_2$SiO$_3$, *etc.*, and conduct a thorough investigation on these compounds using density functional theory (DFT), particularly for their TE applications. To the best of our knowledge, among the suggested alkali metal oxides, K$_2$PbO$_3$ was the first compound to be synthesized back in 1964 by Hoppe and co-workers;[13] later, in the year 1972 the Cs$_2$PbO$_3$ compound was synthesized by Panek *et al.*,[14] and then latterly the Rb$_2$PbO$_3$ was again synthesized in 1977 by Hoppe and Stöver.[15] From these earlier experimental studies, it was found that the K$_2$PbO$_3$, Rb$_2$PbO$_3$, and Cs$_2$PbO$_3$ existed in an orthorhombic structure with space group *Cmc*2$_1$ (no. 36). More recently, in 1982, Brazel and Hoppe synthesized the Li$_2$PbO$_3$ by decomposing K$_2$Li$_6$[Pb$_2$O$_8$] and reported a monoclinic structural symmetry (*C*2/*c* space group) for this compound.[16] The interesting information about the *Cmc*2$_1$ symmetry materials of X$_2$PbO$_3$ is that in these structures, similar to the prototype Na$_2$SiO$_3$, and Na$_2$GeO$_3$, the presence of links between oxygen and Pb-atoms led to the formation of a three dimensional network of a tetrahedral chain of [PbO$_4$].

[a]Department of Physics, Mizoram University, Aizawl-796004, India. E-mail: dibyaprakashrai@gmail.com

[b]Physical Sciences Research Center (PSRC), Department of Physics, Pachhunga University College, Aizawl-796001, India

[c]Department of Physics and Astronomy, College of Science, King Saud University, Riyadh, 11451, Saudi Arabia

[d]Department of Material Science and Nanotechnology, Nepal Academy of Science and Technology (NAST), Khumaltar 44700, Lalitpur, Nepal

The link forms the bridge-oxygen (BO) and non-bridge-oxygen (NBO), where alkali atoms such as X = K, Rb, and Cs are bonded.[17] Therefore, K_2PbO_3 (KPO), Rb_2PbO_3 (RPO), and Cs_2PbO_3 (CPO) are non-centrosymmetric in structure, and consequently exhibit piezoelectric properties. Moreover, in case of Li_2PbO_3 (LPO) and Na_2PbO_3 (NPO), since the compounds are centrosymmetric, they do not possess piezoelectricity.

In the past few decades, experimental and theoretical insights into novel multi-function energy materials especially for TE and piezoelectric applications have become a hot topic among researchers.[18–20] Thermoelectricity and piezoelectricity hold the requisite hallmarks for green energy resources as they produce electricity without any emissions of toxic pollutants. The glass-like materials possessing high mechanical and thermal stability, low lattice thermal conductivity (κ_L), high melting temperatures (T_m), ease of availability, and the cost-effectiveness have made these materials perfect candidates for multi-use energy generators. However, the presence of the toxic Pb-element in our proposed compounds *i.e.*, X_2PbO_3 have made this topic more challenging. From various research articles, it has been observed that the toxicity offered by the Pb-element can be successfully minimized, and the prominent strategies for this include chelation therapy, nano-encapsulation, and *N*-acetylcysteine (NAC).[21–23] A common strategy to reduce toxicity is the substitution of the Pb element with less toxic elements such as Sn and Pb. Since, both elements possess compatible ionic radii and electronic structures, they enable the replacement of Pb without major lattice distortions, while reducing the overall Pb content. Moreover, from a functional perspective, Sn-substitution is particularly attractive for energy-related applications because it retains the narrow band gap and high carrier mobility that are essential for optoelectronic and photocatalytic processes.[24,25] However, for X_2PbO_3 materials, when X moves from Li $\rightarrow$ Cs, the environmental risk of X_2PbO_3 is expected to increase, as larger alkali ions weaken the glass network and facilitate Pb release. To reduce the energy crisis rendered by the global demands for energy sources, thermoelectricity and piezoelectricity could be an innovative approach although their efficiencies are low. From the recent study led by Zosiamliana *et al.*,[26] the TE efficiencies at $T = 1200$ K for Pb-based perovskites such as $PbTiO_3$, $PbZrO_3$, and $PbHfO_3$ were found to be $ZT = 0.64$, 0.66, and 0.61, revealing the suitability of Pb-based materials for TE devices. Also, recent reports reveal the relevancy of glass-like materials such as Na_2SiO_3 and Na_2GeO_3 (the prototype compounds for KPO, RPO, and CPO) for piezoelectric devices, with a response of $e_{33} = 0.22$ C m^{-2} and $e_{33} = 0.91$ C m^{-2}, respectively.[12,27,28] Experimentally and theoretically, only few research studies have been carried out on glass-like materials for TE applications. Recently, an efficiency of $ZT = 0.027$ at $T = 393$ K was reported for Na_2SiO_3 as a graphite/mixture ($CuSO_4$ + CoOH + SiO_2 + Na_2SiO_3)/aluminum by Chira *et al.*[29] Thus, the unmet research area that needs to be addressed is the piezoelectric and TE applications of X_2PbO_3 glass-like materials.

As far as we know, from several literature surveys, only a few experimental and theoretical studies were conducted on these materials. Recently, the photo-catalytic use of these compounds for solar-to-hydrogen conversion was reported by Gelin and colleagues[30] however, this failed to provide a comprehensive insight into the fundamental properties. As a result, the main focus of this work will be on the thorough analysis of the fundamental characteristics of X_2PbO_3 (X = Li, Na, K, Rb, Cs) and their applications for piezoelectric and TE materials employing hybrid-DFT.

2 Computational details

In this work we have performed density functional theory (DFT) calculations as implemented in the CRYSTAL17-code to evaluate the physical properties of X_2PbO_3. In this part of the DFT framework the crystal orbitals are described by the linear combination of Gaussian-type functions (GTF).[31] The atomic centers for all the constituent atoms such as X = lithium (Li), sodium (Na), potassium (K), rubidium (Rb), and caesium (Cs), lead (Pb), and oxygen (O) were described by a revised triple-ζ valence plus polarization (TZVP) basis set.[32,33] In this work, four different exchange–correlation functionals were adopted, namely; (1) the Perdew–Burke–Ernzerhof (PBE) generalized gradient approximation (GGA);[34] global hybrids: (2) Becke 3-parameter Lee–Yang–Parr (B3LYP),[35,36] and (3) PBE with 25% Fock exchange (PBE0);[37] and (4) the range-separated hybrid screened-Coulomb (SC) called HSE06.[38]

The expressions for the employed hybrid functionals are:[39]

$$E_{XC}^{B3LYP} = E_{XC}^{LSDA} + a_0(E_X^{exact} - E_X^{LSDA}) + a_X\Delta E_X^{B88} + a_C\Delta E_C^{PW91} \quad (1)$$

Here, a_0, a_X, and a_C are semi-empirical coefficients, E_{XC}^{LSDA} is the local spin density exchange–correlation, E_X^{exact} is the exact exchange energy, ΔE_X^{B88} is Becke's gradient correction for exchange, and ΔE_C^{PW91} is the Perdew and Wang gradient correction.

$$E_{XC}^{PBE0} = \frac{1}{4}E_X^{HF} + \frac{3}{4}E_X^{PBE} + E_C^{PBE} \quad (2)$$

Here, the full PBE correlation energy and the 3 : 1 ratio of PBE to HF exchange energies determine the PBE0 functional.

$$E_{XC}^{HSE06} = \frac{1}{4}E_X^{SR,HF}(\omega) + \frac{3}{4}E_X^{SR,PBE}(\omega) + E_X^{LR,PBE}(\omega) + E_C^{PBE} \quad (3)$$

where, $\omega = 0.2$ is the screening parameter, $E_X^{SR,HF}$ represents the short-range Hartree–Fock exact exchange functional, $E_X^{SR,PBE}$, and $E_X^{LR,PBE}$ are the short-range, and long-range PBE exchange functionals, respectively, and E_C^{PBE} is the full correlation energy.

For the structural optimizations, an analytical quasi-Newtonian approach combined with Hessian Broyden–Fletcher–Goldfarb–Shanno (BFGS) scheme was used.[40,41] To check the convergence, the gradient components and nuclear displacements with tolerances on their root-mean-square (RMS) were set to 0.0001 and 0.0004 Hartree (Ha), respectively. The accuracy of the convergence criteria was set to the five thresholds which control the overlap and penetration of the Coulomb integrals; the overlap for HF exchange integrals, and the pseudo-overlap were set to (10^{-7}, 10^{-7}, 10^{-7}, 10^{-7}, 10^{-7}, 10^{-14}). The first Brillouin zone integration was performed using a 10 × 10 × 10 *k*-mesh within the Monkhorst–Pack scheme,[42] and an energy convergence criteria of 10^{-7} Ha was considered. Then, to

ensure that the optimized geometries correspond to true minima on the potential energy surface (PES), we conducted an equation-of-state (EOS) analysis on the optimized structures. The total energy as a function of cell volume was examined to confirm that the optimized configurations correspond to the lowest point (global minimum) on the energy–volume curve, thereby validating the structural stability and energetic consistency of the obtained geometries. For the calculation of the physical properties we have set the higher k-mesh of $12 \times 12 \times 12$. For the calculation of the elastic and piezoelectric properties, we have opted for the best suited exchange–correlation functionals depending on the accuracy in reproducing the experimental lattice parameters. To verify the structural stability, we performed an *ab initio* molecular dynamics (AIMD) simulation with an nVT canonical ensemble (calculation details are provided in Section 3.1).[43–45]

For the TE properties calculation, the Boltzmann transport semi-classical equation (BTE) within a rigid band approximation (RBA) using BoltzTraP as implemented in the CRYSTAL17-code was employed.[7,46,47] The wave functions were recalculated at a dense k-mesh of $42 \times 42 \times 42$ within the first Brillouin zone. A constant relaxation time approximation (CRTA) for carriers was assumed for all the investigated compounds, and fixed at $\tau = 10^{-14}$ s (default τ for BoltzTraP-code).

3   Results and discussions

3.1   Structural properties and stability

The structural optimization results using various adopted functionals such as PBE-GGA, B3LYP, HSE06, and PBE0 reveal that the investigated compounds X_2PbO_3 crystallized in monoclinic symmetry ($C2/c$ space group) for X = Li, and Na, and in an orthorhombic structure ($Cmc2_1$ space group) for X = K, Rb, and Cs [see Fig. 1]. The agreements between the calculated lattice constants and the available experimental data for each compounds are presented in Table S1. For LPO, KPO, RPO, and CPO the global hybrid-PBE0 functional is found to be the most relevant functional in reproducing the experimental data with $|\Delta a|$, $|\Delta b|$, and $|\Delta c| < 2\%$, as it is known that the global hybrid-PBE0 functional reproduces better lattice parameters and the electronic band structure of small or large band gap solids. It is important to remain aware that the stability of the studied systems will be impacted if the lattice constant's precision deviates by more than 2%.[26] From the formation energy (E^f) calculations using eqn (4), a negative E^f reveals the ground state structural stabilities for all the considered systems in their corresponding phases, and implies a possible realization of their experimental synthesis. Furthermore, a greater negative E^f is observed for each compound with the PBE0 functional, suggesting this functional is the most favored to acquire the energy ground state. As a result, each compound's optical, elastic, and piezoelectric properties are investigated using the PBE0 functional. However, the electronic and TE properties are explicitly calculated using the four different adopted functionals in order to verify the role played by exchange–correlation functions during the study of TE properties.

$$E^f = \frac{1}{12}[E_{tot} - (4E_X + 2E_{Pb} + 6E_O)] \qquad (4)$$

Here, E_{tot} is total ground state energy, and E_X, E_{Pb}, and E_O are the corresponding single atom ground state energies for the X, Pb, and O atoms. Since there are 12 atoms in the unit cell, the right hand side (RHS) of eqn (4) is divided by 12. To obtain the most stable configurations for all the examined systems, total energies *versus* the unit cell volumes were fitted through the Birch–Murnaghan equation of states (EOS) scheme given by eqn (5) using the PBE0 functional.[49,50] From the depicted smooth parabolic curves in Fig. 2, the energy difference where $E - E_0 = 0$ eV corresponds to the most stable structure.

$$E(V) = E_0 + \frac{9 \times B_0 V_0}{16}\left[\left[\left[\left(\frac{V_0}{V}\right)^{\frac{2}{3}} - 1\right]^3 \times B_0' + \left[\left(\frac{V_0}{v}\right)^{\frac{2}{3}} - 1\right]^2\right. \right.$$
$$\left.\left. \times \left[6 - 4 \times \left(\frac{V_0}{V}\right)^{\frac{2}{3}}\right]\right]\right] \qquad (5)$$

To verify the thermal and dynamic stabilities of the studied systems, we have performed molecular dynamics (MD) simulations for each of the relaxed conventional cell structures (*i.e.*, two times the number of atoms in the unit cell) both at room temperature and at $T = 850$ K, and the phonon dispersion curve calculations. Since MD simulations cannot be performed using the CRYSTAL17-code, throughout this computational process the QuantumATK Q-2019.12 code, which relies on a linear combination of the atomic orbital method (LCAO) with the canonical ensemble (nVT) based on Nosé–Hoover thermostat, was adopted.[51–53] A 12 ps total simulation time with 4 fs time step for room temperature stability and a 5 ps total simulation time for $T = 850$ K were considered during the simulations for all the structures. The graphical representation of the MD simulations (see Fig. 4 and S16) calculated in nVT ensemble where the number of atoms, cell volume, and temperature are constant provides a more realistic insight into the evolution of energies (PE, and KE), and temperature (T). Here, PE and KE represent the sum of energies from non-bonded and bonded
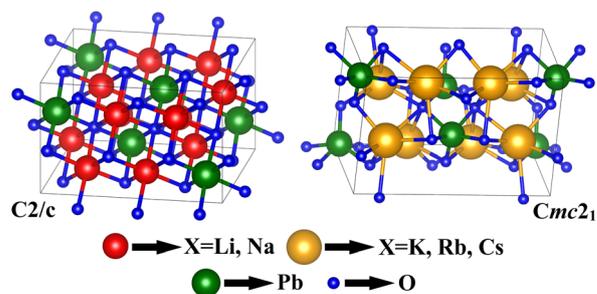

Fig. 1 The $C2/c$ (X = Li, Na), and $Cmc2_1$ (X = K, Rb, Cs) structures of X_2PbO_3 viewed using an external program called VESTA.[48]
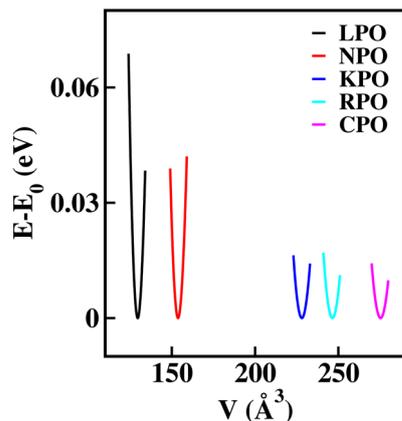
Fig. 2 Energy *vs.* volume curves of X_2PbO_3 (X = Li, Na, K, Rb, Cs) calculated using the Birch–Murnaghan's EOS curve fitting method. Here, E_0 is ground state energy.
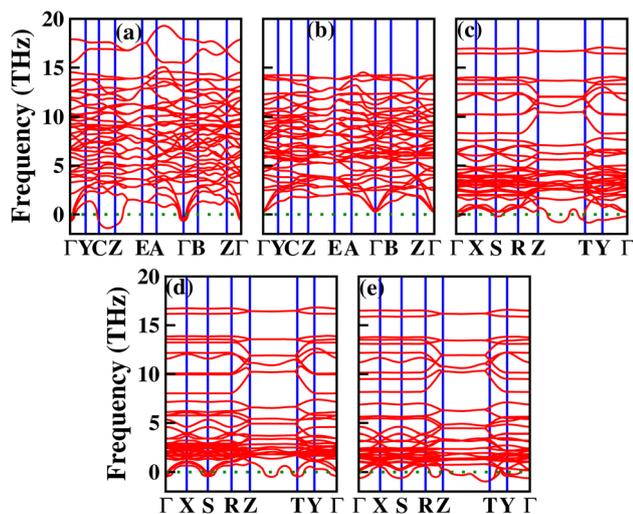

Fig. 3 Phonon dispersion curves of X_2PbO_3: (a) X = Li, (b) X = Na, (c) X = K, (d) X = Rb, and (e) X = Cs.
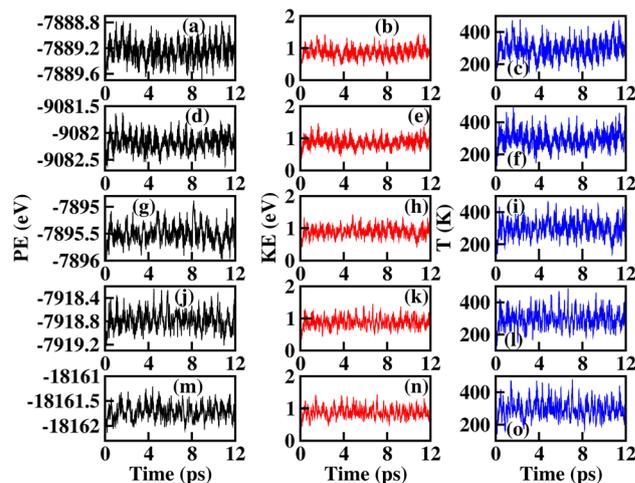

Fig. 4 The potential energy (PE), kinetic energy (KE), and evolution of temperature (T) as a function of time steps calculated using MD simulations based on a nVT-canonical ensemble: (a–c) X = Li, (d–f) X = Na, (g–i) X = K, (j–l) X = Rb, and (m–o) X = Cs.

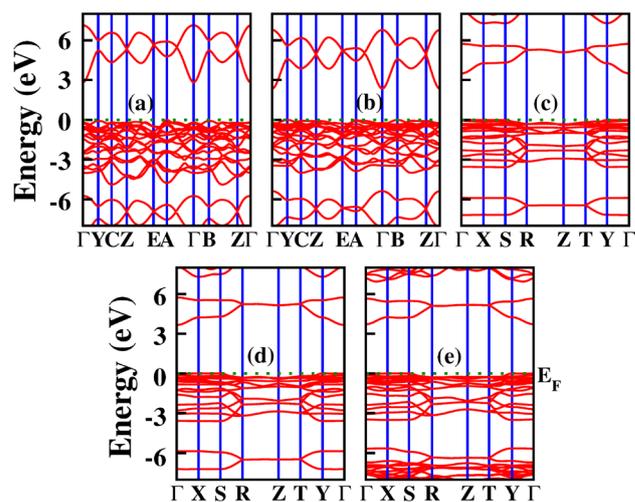**Fig. 5** Calculated band structures for X_2PbO_3 using the PBE0 functional: (a) X = Li, (b) X = Na, (c) X = K, (d) X = Rb, and (e) X = Cs.

interactions, and the heat absorbed by the systems, respectively. The higher evolution of *T* with time suggests more movement of the atoms, thereby resulting in more fluctuation of the KE. The nearly linear fluctuations of PE, KE, and *T* even up to 12 ps time steps reveals the thermal stability for all the investigated materials at room temperature and the nearly linear fluctuation of the MD parameters at *T* = 850 K verified the thermal stability at the higher temperature range. To verify the dynamic stability of the studied systems, we have presented the GGA calculation of the lattice dynamics with their relaxed structures. The graphical representation of the phonon dispersion curve within the first Brillouin zone is shown in Fig. 3. Due to the presence of 24 atoms in a conventional cell, we can have 72 vibrational modes of phonons at any *q*-point, consisting of three acoustic modes and 69 optical modes. The absence of imaginary phonon frequencies for NPO confirms the dynamic stability, while for other systems, imaginary phonon frequencies (≤0.25 THz) at

some *q*-points, suggested that they are dynamically unstable. However, such low imaginary phonon frequency values could arise from numerical noise during the calculation process. Also, negative phonon frequencies in glass-like materials (the generic nature of glass materials) indicate the presence of soft vibrational modes, consistent with their tendency toward amorphous or disordered configurations. They can also partly arise from computational limitations in modeling inherently non-periodic systems using periodic boundary conditions.

3.2 Electronic properties

The emergence of physical properties can be understood by interpreting electronic properties with regard to orbital interactions at the atomic level. In this section, we have studied the electronic properties which includes band structures, density of
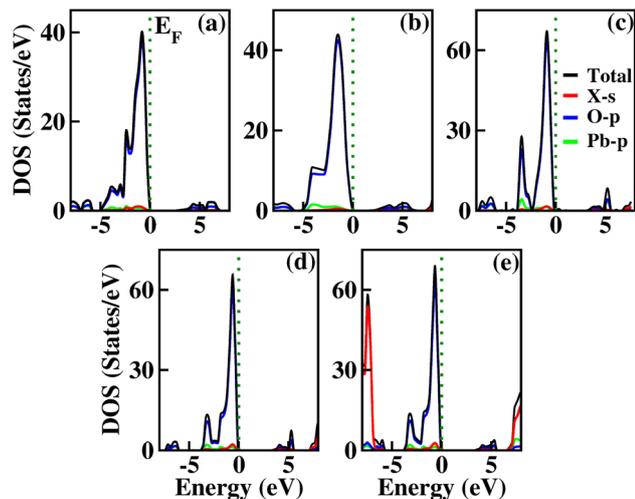
Fig. 6 Calculated DOS for X_2PbO_3 using the PBE0 functional: (a) X = Li, (b) X = Na, (c) X = K, (d) X = Rb, and (e) X = Cs.

states (DOS), and atomic charge transfer (Q_T) using PBE-GGA, B3LYP, HSE06, and PBE0 functionals. The presented band structures, and DOS calculated using the PBE0 functional in Fig. 5 and 6 (for PBE-GGA, B3LYP, and HSE06 see Fig. S1 and S2), and the energy gap (E_g) at the high symmetry points given in Table 1, revealed the indirect semi-conducting band gap nature for LPO, and NPO with the top and bottom of the valence and conduction bands lying at the A and Γ-symmetry points. For KPO, RPO, and CPO, E_g are along the Γ-symmetry suggesting a direct band gap semiconductor behavior. The incorporation of hybrid functional flavors during the electronic properties calculations has a significant effect on the E_g due to the shifts in the energy levels, however, the energy band profiles are preserved. Evidently, from Table 1, since the $C2/c$-X_2PbO_3 compounds have distinct local coordination environments and Pb–O network conductivities compared to those of the $Cmc2_1$-X_2PbO_3 compounds, in the $C2/c$-X_2PbO_3 structures, the Pb–O bonds experience stronger octahedral distortion and shorter

Pb–O bond lengths, leading to enhanced Pb–O orbital overlap. This stronger hybridization raises the valence band maximum and narrows the E_g. Hence, within the $C2/c$ structures, the smaller cation X = Li experiences increasing overlap and reducing E_g compared to X = Na, while in the $Cmc2_1$-X_2PbO_3 structures, there is a less distorted Pb–O framework and more symmetric coordination geometry. They have reduced Pb–O orbital overlap and weakened Pb–O hybridization, which lowers the valence band maximum and increases the E_g. Thus, within $Cmc2_1$ structures, E_g increases with increasing ionic radius because the structure becomes more open and less covalently bonded. Comparing the obtained E_g with the recent report led by Gelin et al.,[30] where E_g were recorded for the $C2/c$ symmetry of Li_2PbO_3, $P6_3/mmc$ symmetry of K_2PbO_3, $Pnma$ symmetry of Rb_2PbO_3, and $Cmc2_1$ symmetry of Cs_2PbO_3 using GGA and GGA+U approximations, one can find that these reported E_g accord well with our results.

Insight into the general distribution of electronic states at different energy levels and the electronic charge distributions upon the formation of bonds are gained through the analysis of DOS and Mulliken population analysis.[54] From the DOS plots, it is comprehensible that for all the studied compounds, the main contributing states near the Fermi level (E_F) along the valence band region are from the O-p states, while the major contributions along the conduction region are from the complex hybridized states of X-s, Pb-p, and O-p, which are analogous to those closely related glass-like materials such as Li_2SiO_3, Na_2SiO_3, Li_2GeO_3, and Na_2GeO_3.[12,27,55,56] For each compound, from the relatively greater atomic concentrations of NBO than BO, and from the simple altercation of on-site Coulomb repulsion, the NBO-p orbitals which have greater energy (or lower binding energy) are likely to have larger valence charges than BO-p orbitals. Therefore, among the two prominent DOS peaks along the valence region found between −5 eV and 0 eV, the first peak which is closer to the E_F is mainly from NBO-p contributions, while the second peak which is at the lower energy region is predominantly contributed by BO-p. Furthermore, from the data of the Mulliken population analysis of the relative atoms' charge distributions calculated from different adopted functionals presented in Table 1, the X and Pb atoms transfer charges while the NBO and BO atoms accumulate them for all the considered systems. By establishing a correlation between the charge transfer and DOS, it is possible to clarify the impact of various functionals on the electronic properties calculation. For LPO, and NPO, from the DOS plots it is possible to notify that the total DOS (TDOS) contribution near E_F is comparatively higher with the PBE-GGA functional when compared to other adopted functionals. This is mainly due to a significant change in Q^T between the PBE-GGA and hybrid functionals' calculated results. With hybrid functionals the charge accumulated by the BO and NBO becomes larger suggesting a lower number of unoccupied states, which subsequently reduces the TDOS contribution around E_F. However, for KPO, RPO, and CPO an opposite phenomenon of the PBE-GGA estimated TDOS exhibiting a lower contribution near E_F than those hybrid functionals employed is observed, even-though Q^T for BO and NBO becomes larger with hybrid functionals. The structural arrangements of

Table 1 Electronic band gap (E_g) (in eV), and atomic charge transfer (Q_T) (in $|e|$) using Mulliken population analysis for X_2PbO_3 (X = Li, Na, K, Rb, Cs)

X	E_g	Q_X^T	Q_{Pb}^T	Q_{BO}^T	Q_{NBO}^T	E_g	Q_X^T	Q_{Pb}^T	Q_{BO}^T	Q_{NBO}^T
			PBE-GGA					**B3LYP**		
Li	0.88	0.54	1.71	−0.95	−0.92	2.27	0.65	1.99	−1.10	−1.09
Na	0.53	0.74	1.49	−1.01	−0.98	1.83	0.82	1.76	−1.15	−1.12
K	1.23	0.71	1.34	−0.93	−0.92	2.94	0.75	1.55	−1.01	−1.01
Rb	1.45	0.77	1.27	−0.95	−0.93	3.08	0.81	1.47	−1.03	−1.02
Cs	1.53	0.77	1.24	−0.95	−0.92	3.13	0.82	1.43	−1.03	−1.02
			HSE06					**PBE0**		
Li	2.23	0.61	2.01	−1.08	−1.07	2.82	0.61	2.04	−1.09	−1.08
Na	1.79	0.81	1.77	−1.15	−1.12	2.34	0.82	1.80	−1.16	−1.13
K	2.84	0.75	1.57	−1.03	−1.03	3.50	0.75	1.59	−1.03	−1.03
Rb	3.02	0.82	1.50	−1.05	−1.04	3.67	0.82	1.51	−1.05	−1.04
Cs	3.09	0.81	1.47	−1.03	−1.02	3.72	0.81	1.48	−1.03	−1.03

the materials can provide insight into the reason behind this behavior. The X–BO and X–NBO bond lengths in the $C2/c$ symmetry compounds (*i.e.*, X = Li and Na) are identical, while they are unequal in the $Cmc2_1$ symmetry compounds (*i.e.*, X = K, Rb, and Cs). The difference in the structural arrangements of these materials for $C2/c$ and $Cmc2_1$ symmetry compounds is the key factor for the non-centrosymmetric nature of the KPO, RPO, and CPO compounds.

Fig. S15 illustrates the two-dimensional differential charge density map for the investigated compounds, providing profound insights into the charge distribution among the X–BO/NBO, Pb–BO/NBO, and X–Pb interactions. The visualization highlights charge depletion in red and charge accumulation in blue, reflecting the redistribution of electron density within the system. This charge rearrangement plays a crucial role in elucidating the relationship between charge transfer mechanisms and electronic band structures, particularly concerning electron transitions from the valence band to the conduction band through the electronic band gap. In each case, X and Pb atoms predominantly act as electron donors, leading to localized charge depletion in their vicinity. In contrast, oxygen atoms, due to their higher electronegativity, attract electron density, resulting in significant charge accumulation around O-sites. This pronounced electron localization at oxygen centers underscores their function as electron-rich species, thereby influencing the overall electronic structure and bonding nature of the studied materials. The observed charge density differences align well with other electronic properties, including the calculated density of states (DOS) and Mulliken population analysis. Furthermore, while no substantial variations are observed between the employed functionals, noticeable differences arise when comparing the $C2/c$-X_2PbO_3 and $Cmc2_1$-X_2PbO_3 phases. Specifically, the $C2/c$-X_2PbO_3 structure exhibits a more pronounced presence of red and blue regions than the $Cmc2_1$-X_2PbO_3 phase, indicating stronger charge transfer interactions. This suggests a more significant charge redistribution in the $C2/c$ system, highlighting its enhanced electronic polarization and bonding characteristics. Also, the analysis of the electronic structure has been expanded to correlate the observed trends with underlying Pb–O bonding and orbital hybridization. The variations in E_g are attributed to the interplay between Pb–O covalency, cation size, and crystal symmetry, where enhanced Pb–O hybridization in the $C2/c$ phase narrows the E_g, while reduced overlap in the $Cmc2_1$ phase widens it.[57] Charge-density and DOS analyses confirm the dominant Pb-6s/ O-2p contributions near the band edges. These electronic features govern carrier transport and suggest that structural or compositional tuning could optimize the X_2PbO_3 compounds for thermoelectric, sensor, or optoelectronic applications.[58]

3.3 Optical properties

To interpret the interaction between electromagnetic radiation and the studied X_2PbO_3 materials, we have explored the optical properties by calculating the complex dielectric constants (ε), extinction coefficient, refractive index, reflectivity, and absorption coefficient as a function of photon energy using the PBE0

functional. It is known that at higher frequencies, ε is divided into two parts, namely; the real part (ε_1), and the imaginary part (ε_2) [see eqn (6)].[59]

$$\varepsilon = \varepsilon_1 + i\varepsilon_2 \tag{6}$$

For calculating other optical parameters like extinction coefficient (k), refractive index (η), reflectivity (R), and absorption coefficient (α), the employed formulae are:

$$k(\omega) = \sqrt{\frac{(\varepsilon_1{}^2 + \varepsilon_2{}^2)^{\frac{1}{2}} - \varepsilon_1}{2}} \tag{7}$$

$$\eta(\omega) = \sqrt{\frac{(\varepsilon_1{}^2 + \varepsilon_2{}^2)^{\frac{1}{2}} + \varepsilon_1}{2}} \tag{8}$$

$$R(\omega) = \frac{(1-\eta)^2 + k^2}{(1+\eta)^2 + k^2} \tag{9}$$

$$\alpha(\omega) = \frac{2\omega\kappa(\omega)}{c} \tag{10}$$

The ε_1 which is closely interrelated with η determines the amount of material polarization and dispersion of electromagnetic radiation when interacting with the material surface [see Fig. 7(a) and (d)]. The calculated static real dielectric constants $\varepsilon_1(0)$ are in the order of LPO > NPO > CPO > RPO > KPO, with values in the range of 2.80 to 3.90 arb. unit, for all x, y, and z-axes. The $\varepsilon_1(0)$ for the investigated materials are all higher than those of glass-like materials such as Na_2SiO_3, whose values is in the range of 1.00 to 1.40 arb. unit, while for Na_2GeO_3, $\varepsilon_1(0)$ is comparable with X_2PbO_3, whose value is ~3.00 arb. unit.[12,27] Along the x-axis, the first prominent peaks for ε_1^x are found within 3.0 to 4.5 eV and undergo blue shifting as X goes from Na → Li → Cs → Rb → K. This indicates that the maximum probable interaction with electromagnetic radiation not only differs but also varies across frequency ranges for each compound. Among all the investigated systems, higher static refractive index $\eta(0)$ values are observed for X = Li, and Na than when X = K, Rb, and Cs, with $\eta(0)$ values ranging from 1.5 to 2.0, revealing that they are translucent in nature. Corresponding to ε_1, the curves of η show similar trends. The decreasing refractive indices at higher photon energy region *i.e.*, beyond 8 eV, reveals that the electromagnetic radiation no longer has sufficient energy to interact electronically with the material's electron.

The ε_2 which is closely related to the k and α corresponds to the inter-band transition between the valence and conduction bands. From Fig. 7(b), on analyzing the direction-wise behavior of ε_2, it is noticeable that ε_2 is highly anisotropic in nature. Clearly, one can find two prominent peaks of ε_2 for each compound along the x and z-axes, and three distinct peaks in the y-axis. Along the x-axis, the first prominent peaks of ε_2^x are blue shifted as X moves from Li → K → Cs → Rb → Na. The extinction coefficient (k) which determines the materials capacity to absorb radiation of a specific wavelength is depicted in Fig. 7(c). The obtained minimum threshold energies for X = Li,
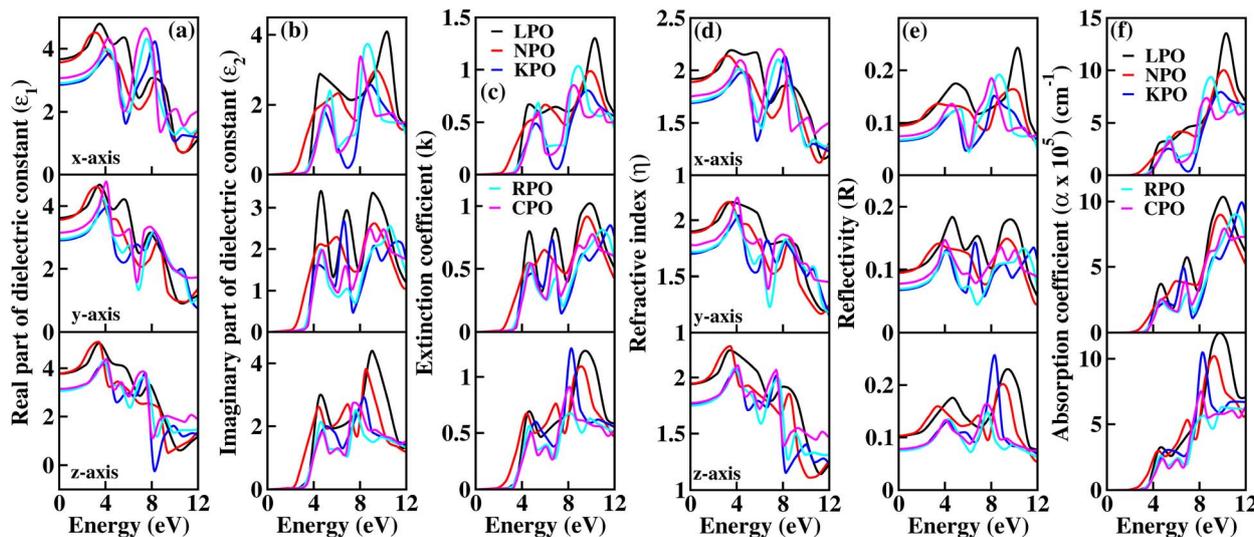
Fig. 7 Calculated optical properties of X_2PbO_3 (X = Li, Na, K, Rb, Cs) using the PBE0 functional: (a) real part of dielectric constant (ε_1), (b) imaginary part of dielectric constant (ε_2), (c) extinction coefficient (k), (d) refractive index (η), (e) reflectivity (R) and (f) absorption coefficient (α).

Na, K, Rb, and Cs are 3.51, 2.33, 3.46, 3.62, and 3.69, respectively, and correspond to their respective optical band gaps. Meanwhile, when compared to other glass-like materials such as Na_2SiO_3 ($\varepsilon_2 = 2.5$ eV) and Na_2GeO_3 ($\varepsilon_2 = 3.2$ eV), our investigated materials exhibit a higher optical threshold energy. This indicates that these materials are likely to exhibit a stronger response in the higher visible-to-ultraviolet (vis–UV) spectral region. The optical band gaps for X = Na, K, Rb, and Cs, agree well with the first direct electronic transition from the top of the valence band (O-p state, specifically NBO-p state) to the bottom of the conduction band (X-s state) along the Γ-symmetry. However, for X = Li the optical band gap is due to the direct electron transition from the third band of the valence band (O-p state) to the bottom of the conduction band (Li-s state) along the Γ-symmetry. Along the x-axis, the respective first prominent peaks of k^x for X = Li, Na, K, Rb, and Cs are located within the region 4.50 to 6.00 eV. This corresponds to the first inter-band transition between the valence band and conduction band along the A-symmetry point for LPO, and NPO, and for KPO, RPO, and CPO, the transition is along the Z-symmetry.

The main motive for exploring the optical properties is to determine the reflectivity and the optical absorption [see Fig. 7(e) and (f)]. From the reflectivity spectra as a function of the photon energy, similar to the other optical property parameters, a highly anisotropic trending of the reflectivity curves is found for each compound. The static reflectivity (R(0)) values being lower than 0.1 along x, y, and z-axes reveals the semi-conducting behavior of the considered systems. Between 0 and 4.0 eV photon energy, each compound shows increasing reflectivity with energy and then beyond 4.0 eV, drastically fluctuating reflectivity profiles are observed. Since the maximum reflectivity even at higher photon energy regions (i.e., within the ultra-violet region) is less than 25%, it indicates that the examined materials should be good high energy electromagnetic radiation absorbers rather than reflectors. From the curve of the absorption coefficient as a function of photon energy which is consistent with other optical properties

such as ε_2 and k, one can observe a rapid increase of absorption from ~3.0 eV photon energy. For each compound, along the x, y, and z-axes the first promising optical absorptions are in the region of 4.0 to 5.0 eV. Since the most active optical absorptions for all the studied materials fall within the UV-region with $\alpha > 1 \times 10^5$ cm^{-1}, these compounds might be a potential candidates for optical materials that can serve as UV-radiation shielding materials.

3.4 Elastic properties

For practical applicability particularly in the field of piezoelectric and TE applications, the crystalline materials' strength which is interpreted from the elastic properties plays a key role. In this regard, we report the elastic constant (C_{ij}) and other mechanical properties of X_2PbO_3. Since the investigated compounds exist in a monoclinic phase for X = Li, and Na, and orthorhombic phase for X = K, Rb, and Cs, we have ten elastic constants [see Table 2]. The necessary and sufficient conditions for the studied systems to become mechanically stable called Born criteria are given below:[60,61]

For the monoclinic phase, the criteria are:

$$C_{11}, \ C_{22}, \ C_{33}, \ C_{44}, \ C_{55}, \ C_{66} > 0$$
$$C_{44}C_{66} - 2C_{46} > 0$$
$$C_{11} + C_{22} + C_{33} + 2(C_{12} + C_{13} + C_{23}) > 0$$
$$C_{22} + C_{33} - 2C_{23} > 0 \tag{11}$$

For the orthorhombic phase, the criteria are:

$$C_{11}, \ C_{22}, \ C_{33}, \ C_{44}, \ C_{55}, \ C_{66} > 0$$
$$C_{11}C_{22} > C_{12}^2$$
$$\left[C_{11}C_{22}C_{33} + 2C_{12}C_{13}C_{23} - C_{11}C_{23}^2 - C_{22}C_{13}^2 - C_{33}C_{12}^2\right] > 0 \tag{12}$$

Since the calculated elastic constants C_{ij} of the X_2PbO_3 compounds meet the above mentioned stability criteria, they are mechanically stable. In Table 2, the C_{11}, C_{22}, and C_{33}

Table 2 Calculated elastic constants C_{ij} (in GPa) of X_2PbO_3 (X = Li, Na, K, Rb, Cs) using the PBE0 functional

X	C_{11}	C_{22}	C_{33}	C_{44}	C_{55}	C_{66}	C_{12}	C_{13}	C_{23}	C_{46}
Li	155.99	202.51	230.62	67.19	47.69	54.42	50.38	34.38	67.17	−11.63
Na	136.52	170.85	183.30	70.52	49.14	59.95	46.12	40.96	59.79	8.06
K	83.28	57.12	131.37	25.30	9.52	16.44	32.04	13.19	31.84	0.00
Rb	74.45	63.81	117.98	26.76	7.17	13.32	31.59	11.35	31.19	0.00
Cs	74.09	62.86	102.86	26.99	2.52	13.78	30.15	16.55	26.87	0.00

Table 3 Elastic moduli (bulk modulus (B), Young's modulus (Y), and shear modulus (G) all in GPa units), and Poisson's ratio (ν) (unitless) using the PBE0 functional. Here, the subscripts V, R and, H represent Voigt, Reuss and Hill assumptions, respectively

X	B_V	B_R	B_H	Y_V	Y_R	Y_H	G_V	G_R	G_H	ν_V	ν_R	ν_H
Li	99.22	87.11	93.17	156	132.71	144.36	63.01	53.25	58.13	0.24	0.25	0.24
Na	87.16	80.48	83.82	144.10	134.08	139.09	58.84	54.85	56.84	0.22	0.22	0.22
K	47.32	44.56	45.94	59.89	45.85	52.95	23.23	17.26	20.24	0.29	0.33	0.31
Rb	44.95	43.63	44.29	55.83	40.16	48.14	21.59	14.91	18.25	0.29	0.35	0.32
Cs	42.98	42.26	42.62	51.37	23.86	38.14	19.74	8.49	14.11	0.30	0.4	0.35

Table 4 Pugh's ratio (k) (unitless) in Hill's approximation, velocity of sound (v) (in km s^{-1}), density (ρ) (in g cm^{-3}), Kleinman coefficient (ζ) (unitless), anisotropic factor (A_{an}) (unitless), machinable factor (μ_m) (unitless), melting temperature (T_m) (in K), Debye temperature (Θ) (in K), and Frantsevich ratio (G/B). Here, the subscripts t, l and av represent transverse, longitudinal and average velocities, respectively

X	k_H	v_t	v_l	v_{av}	ρ	ζ	A_{an}	μ_m	$T_m \pm 300$	Θ	G/B
Li	1.60	2.89	4.86	3.20	6.94	0.47	1.96	1.39	1475.06	432.07	0.62
Na	1.47	2.95	4.94	3.26	6.53	0.48	2.29	1.19	1359.97	415.51	0.65
K	2.27	2.04	3.87	2.28	4.87	0.52	1.77	1.82	1045.27	254.71	0.43
Rb	2.43	1.78	3.46	1.99	5.74	0.56	1.75	1.65	993.07	216.38	0.41
Cs	3.02	1.50	3.12	1.69	6.29	0.54	2.06	1.58	990.95	177.17	0.33

determine the system's stiffness in relation to fundamental stresses while C_{44}, C_{55}, and C_{66} give their resistance against shear deformation. From the constants C_{11}, C_{22}, and $C_{33} \gg C_{44}$, C_{55}, and C_{66} it can be understood that the compounds X_2PbO_3 tend towards greater resistance to axial compression than shear deformation, which is re-confirmed by the fact that bulk moduli (B) are greater than shear moduli (G). Also, the high dissimilarity values of C_{ij} reveals that each compound possesses anisotropic single-crystal elastic behavior. Additionally, our results for the elastic constants also suggest that among the investigated X_2PbO_3 materials, the $C2/c$-X_2PbO_3 structured compounds show greater anisotropic elastic nature compared to those with the $Cmc2_1$-X_2PbO_3 structure. Herein, the elastic moduli: the bulk modulus (B), Young's modulus (Y) and shear modulus (G) given in Table 3 are determined in terms of Voigt, Reuss, and Hill assumptions, which measure the uniform strain, uniform stress, and their average, respectively.[62–64] The larger atomic size of X as it goes from Li → Na for the $C2/c$ structure and from K → Rb → Cs for the $Cmc2_1$ structure reduces the incompressibility and resistance to volume changes due to the increasing lattice parameters which subsequently increases the inter-atomic distances, and consequently, causes B to reduce. In a similar vein, the resulting Y and G likewise decrease correspondingly. This implies that the studied compounds are soft, flexible, or easier to stretch as X moves

down the group. Analyzing the brittleness or ductility based on calculations of Poisson's (ν) (estimated using Voigt, Reuss, and Hill assumptions) and Pugh's ratios (k) (estimated by Hill assumption only) evaluated using eqn (13) and tabulated in Tables 3 and 4, indicates that the $C2/c$-X_2PbO_3 structured compounds are brittle in nature, while the $Cmc2_1$-X_2PbO_3 structured compounds are ductile. The ductility behavior is in the order of CPO > RPO > KPO > ($k = 1.75$ or $\nu = 0.28$) > LPO > NPO, where $k = 1.75$ and $\nu = 0.28$ are the critical values for Pugh's ratio and Poisson's ratio such that the materials become ductile.

$$\nu = \frac{Y}{2G} - 1$$
$$k = \frac{B}{G} \tag{13}$$

The information about internal deformation stability and anisotropic factors can be gained through the Kleinman coefficient (ζ) and elastic anisotropic factor (A_{an}) calculated using eqn (14) and presented in Table 4.[65,66] The ζ which is in the range $0 \leq \zeta \leq 1$ represents stretching and bending of bonds; a value of ζ closer to 1 indicates a negligible contribution of bond stretching. Clearly, for $C2/c$-X_2PbO_3 structured compounds, the mechanical strength is mostly contributed by

bond stretching, while for $Cmc2_1$-X_2PbO_3 structured compounds it is mainly due to the contribution from bending of bonds. Since the obtained A_{an} is larger than 1 for all the considered systems, they are highly anisotropic in nature (A_{an} = 1 represents isotropic).

$$\zeta = \frac{C_{11} + 8C_{12}}{7C_{11} + 2C_{12}}$$

$$A_{an} = \frac{4C_{11}}{C_{11} + C_{33} - 2C_{13}} \quad (14)$$

In this novel work, the main requirement for calculating elastic properties is to check the material's average sound velocity (v_{av}) determined from the transverse and longitudinal velocities (v_t and v_l), and the Debye temperature (Θ) calculated using eqn (15) and (16):[67–69]

$$v_{av} = \left[\frac{1}{3} \left(\frac{1}{v_l^3} + \frac{2}{v_t^3} \right) \right]^{-\frac{1}{3}} \quad (15)$$

where, $v_l = \sqrt{\frac{3B + 4G}{3\rho}}$ and $v_t = \sqrt{\frac{G}{\rho}}$. Here, ρ is density.

$$\Theta = \frac{h}{k} \left(\frac{3nN_A\rho}{4\pi M} \right)^{\frac{1}{3}} v_{av} \quad (16)$$

where, h is the Planck's constant, k the Boltzmann constant, n the number of atoms per formula unit, N_A is Avogadro's number and M the molecular mass.

From the results presented in Table 4, we observe a decreasing v_{av} and Θ when X moves from Li → Na → K → Rb → Cs which is mainly due to the increasing atomic masses. For the $Cmc2_1$-X_2PbO_3 structures, the reported v_{av} are lower than those analogous compounds such as Na_2SiO_3, and Na_2GeO_3

with v_{av} = 4.02 km s^{-1} and 3.19 km s^{-1}, respectively.[28] As sound velocities are inversely proportional to the density [see eqn (15)], the larger values of ρ for the investigated compounds have resulted in the slower v_{av} when compared with the Na_2SiO_3 and Na_2GeO_3 glass-like materials.[12,27,28] The Debye temperature being higher for the $C2/c$-X_2PbO_3 structures than the $Cmc2_1$-X_2PbO_3 structures suggests a greater number of active phonon modes in the $C2/c$-X_2PbO_3.

For the application of any compounds in practice, particularly in the area of piezoelectric and TE applications, machinable factor (μ_m), Frantsevich ratio (G/B), and melting temperature (T_m) play a key role.[70] The μ_m calculated by employing eqn (17) suggests that the investigated X_2PbO_3 compounds exhibit an acceptable level of machinability with lower feed forces and intermediate lubricating properties which makes them a potential candidate for piezoelectric materials. The high T_m and low Frantsevich ratio also reveal that these compounds could be a future TE materials which can be utilized at high temperatures.

$$\mu_m = \frac{B}{C_{44}}$$

$$T_m = (553 + 5.91C_{11}) \pm 300 \quad (17)$$

3.5 Thermodynamic properties

Knowledge of the state of any system in terms of their energy can be gained through thermodynamic properties calculations. In this regard, we have reported the properties for X_2PbO_3 such as the constant volume specific heat (C_V), change in vibrational internal energy (E_{vib}), vibrational entropy (S_{vib}), vibrational
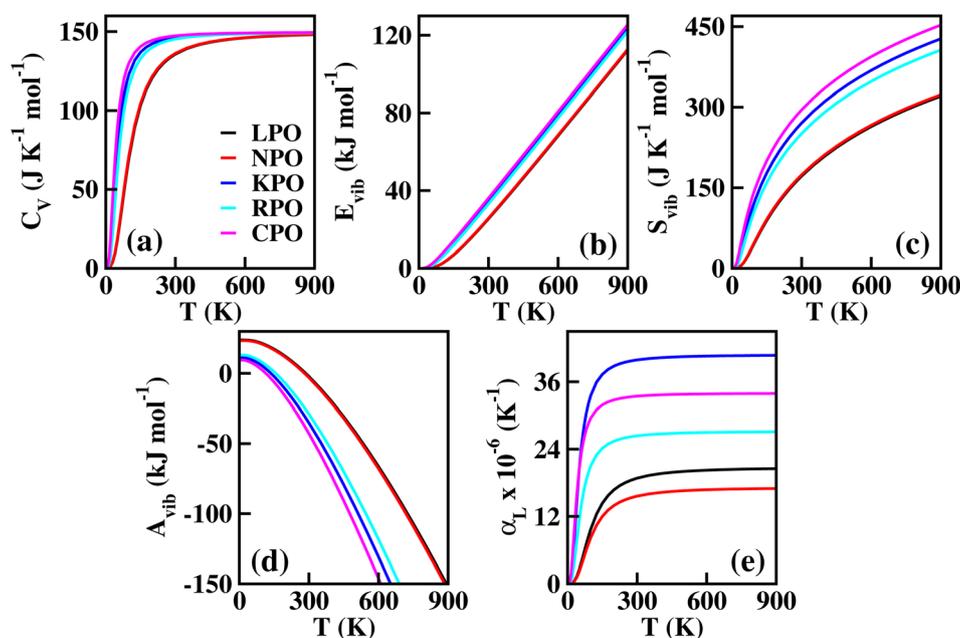

Fig. 8 Calculated thermodynamic properties using GGA formalism: (a) constant-volume heat capacity C_V (J K^{-1} mol^{-1}), (b) change in vibrational internal energy E_{vib} (kJ mol^{-1}), (c) vibrational entropy S_{vib} (J K^{-1} mol^{-1}), (d) vibrational Helmholtz free energy A_{vib} (kJ mol^{-1}), and (e) linear thermal expansion coefficient α (K^{-1}) as a function of temperature.

Helmholtz free energy ($A_{\rm vib}$), and the linear thermal expansion coefficient ($\alpha_{\rm L}$) as a function of temperature based on the quasi-harmonic Debye model (eqn (18)).[71-74] From this model,

$$C_{\rm V} = 3nk\left[4D\left(\frac{\Theta}{T}\right) - \frac{3\Theta/T}{{\rm e}^{\Theta/T} - 1}\right]$$

$$E_{\rm vib}(T) = \sum_i R\Theta_i \frac{1}{\exp(\Theta_i T) - 1}$$

$$S_{\rm vib} = nk\left[4D\left(\frac{\Theta}{T}\right) - 3\ln\left(1 - {\rm e}^{-\Theta/T}\right)\right] \quad (18)$$

$$A_{\rm vib} = nkT\left[\frac{9}{8}\frac{\Theta}{T} + 3\ln\left(1 - {\rm e}^{-\Theta/T}\right) - D(\Theta/T)\right]$$

$$\alpha_{\rm L} = \frac{\gamma C_{\rm V}}{B_{\rm T}V}$$

Here, D is the Debye integral, γ Gruneisen parameter,[75] and $B_{\rm T}$ isothermal bulk modulus defined as,

$$D(y) = \frac{3}{y^3}\int_0^y \frac{x^3}{{\rm e}^x - 1}{\rm d}x$$

$$\gamma = \frac{3(1+\nu)}{2(2-3\nu)} \quad (19)$$

$$B_{\rm T} = -V\left(\frac{\delta P}{\delta V}\right)_{\rm T}$$

where, ν is the Poisson's ratio.

The intrinsic disorderliness which provides the degree of randomness within the studied systems can be determined from the study of their vibrational entropy ($S_{\rm vib}$). From Fig. 8(c), it can be seen that the $C2/c$-X$_2$PbO$_3$ compounds have lower $S_{\rm vib}$ than those compounds with $Cmc2_1$-X$_2$PbO$_3$ structures. This reveals that in $Cmc2_1$-X$_2$PbO$_3$ compounds, the amounts of thermodynamic potential (thermal energy) available for doing useful work are higher than in the $C2/c$-X$_2$PbO$_3$ compounds. The deviation in $S_{\rm vib}$ between the monoclinic and orthorhombic structures of X$_2$PbO$_3$ is mainly due to the variation in the structural and atomic arrangement, and the change in the X-atom component. Also, the increasing $S_{\rm vib}$ for each compound with T suggests more vibrational states become available or accessible when the temperature escalates. In $C2/c$-X$_2$PbO$_3$ compounds, since the arrangement of atoms especially the bonding between alkali atoms with BO and NBO are identical, nearly equivalent $S_{\rm vib}$ curves are obtained. Whereas, for the $Cmc2_1$-X$_2$PbO$_3$ compounds, the X bonding with BO and NBO are in different arrangements which leads to different internal energy contributions, thus showing distinct thermodynamic properties. Additionally, the values of $A_{\rm vib}$ [see Fig. 8(d)] for the $Cmc2_1$-X$_2$PbO$_3$ compounds being lower than those of the $C2/c$-X$_2$PbO$_3$ compounds re-confirms the higher availability of thermal energy for doing useful work in the $Cmc2_1$-X$_2$PbO$_3$ structures. In Fig. 8(b), a linearly increasing $E_{\rm vib}$ with T for both the $C2/c$ and $Cmc2_1$-X$_2$PbO$_3$ structured compounds are observed. This is due to the gradual rising of atoms' kinetic energy with the continuously increasing heat, which leads to more atomic vibrations. This subsequently results in a continuous escalation of vibrational internal energy.

Comprehension of the lattice vibrational characteristics comes from the study of specific heat ($C_{\rm V}$) which is one of the focal points for thermodynamic properties' investigation. The $C_{\rm V}$ curves as a function of temperature for X$_2$PbO$_3$ materials are presented in Fig. 8(a). Evidently, the curves of $C_{\rm V}$ showed similar trending to the nature of other thermodynamic properties parameters plots' mentioned above. The higher value of $C_{\rm V}$ for $Cmc2_1$-X$_2$PbO$_3$ structures reveals more heat can be stored with a small gradation in the temperature compared to the same for $C2/c$-X$_2$PbO$_3$ structures. At low temperatures ($T \ll \Theta$), the $C_{\rm V}$ curves for each compound vary proportionally to T^3, $i.e.$, it follows the Debye's T^3 law [see eqn (20)],

$$C_{\rm V} = \frac{12}{5}\pi^4 nR\left(\frac{T}{\Theta}\right)^3 \quad (20)$$

However, at high temperatures ($T \gg \Theta$), the $C_{\rm V}$ tends to Dulong–Petit limit [see eqn (21)],

$$C_{\rm V} \simeq 3nR \quad (21)$$

where $R = 8.314$ J K^{-1} mol^{-1} is the universal gas constant.

An analysis of the linear thermal expansion coefficient ($\alpha_{\rm L}$) which is closely related to the Young's modulus estimated in the Voigt assumption (uniform strain assumption), yields information about the relationship between the strain that any material endures as a temperature varies. Evidently, from the $\alpha_{\rm L}$ plot presented in Fig. 8(e), one can find that the expansion experienced by the $C2/c$-X$_2$PbO$_3$ compounds is nearly twofold to threefold lower than that of the $Cmc2_1$-X$_2$PbO$_3$ compounds. The fact that the Young's modulus is lower in $Cmc2_1$-X$_2$PbO$_3$ compounds than $C2/c$-X$_2$PbO$_3$ compounds is a key factor for obtaining higher $\alpha_{\rm L}$ for $Cmc2_1$-X$_2$PbO$_3$ structures. A comparison of the thermodynamic parameters ($S_{\rm vib}$, $C_{\rm V}$ and $\alpha_{\rm L}$) for the investigated compounds with some other glass-like materials such as Na$_2$SiO$_3$ and Na$_2$GeO$_3$ is given in Table 5. Clearly, the investigated compounds are thermally more stable at room temperature since they exhibit higher $S_{\rm vib}$ and $C_{\rm V}$ than those of the Na$_2$SiO$_3$ and Na$_2$GeO$_3$ glass-like materials. Also, the lower expansion coefficient of X$_2$PbO$_3$ than Na$_2$GeO$_3$ reveals that the continuous increasing heat will have a reduced effect on the studied X$_2$PbO$_3$ when compared with Na$_2$GeO$_3$.

Table 5 Comparison table of $S_{\rm vib}$ (in J K^{-1} mol^{-1}), $C_{\rm V}$ (in J K^{-1} mol^{-1}), and $\alpha_{\rm L}$ (in K^{-1}) at $T = 300$ K for X$_2$PbO$_3$ (current work), Na$_2$SiO$_3$ and Na$_2$GeO$_3$

Compounds	$S_{\rm vib}$	$C_{\rm V}$	$\alpha_{\rm L}$
This work			
$C2/c$-Li$_2$PbO$_3$	167.26	134.59	18.55×10^{-6}
$C2/c$-Na$_2$PbO$_3$	170.72	135.77	15.35×10^{-6}
$Cmc2_1$-K$_2$PbO$_3$	265.76	145.77	39.59×10^{-6}
$Cmc2_1$-Rb$_2$PbO$_3$	248.48	144.59	26.21×10^{-6}
$Cmc2_1$-Cs$_2$PbO$_3$	291.68	146.35	33.18×10^{-6}
Other's work			
$Cmc2_1$-Na$_2$SiO$_3$ (ref. 76)	112.50	109.50	—
$Cmc2_1$-Na$_2$GeO$_3$ (ref. 12)	163.50	133.90	2.25×10^{-5}

Table 6 Total direct (e_{iv} in C m^{-2} unit) and converse (d_{iv} in pm V^{-1} unit) piezoelectric properties of X_2PbO_3 (X = K, Rb, Cs) using the PBE0 functional computed based on a Berry-phase numerical approach

	Direct					Converse				
X	e_{31}	e_{32}	e_{33}	e_{24}	e_{15}	d_{31}	d_{32}	d_{33}	d_{24}	d_{15}
K	0.32	−0.51	0.30	−0.29	0.29	9.70	−17.41	5.49	−11.53	30.90
Rb	−0.38	0.45	−0.28	0.20	−0.18	−10.63	14.86	−5.24	7.55	−24.71
Cs	−0.01	−0.03	0.16	0.02	0.00	−0.11	−1.13	1.83	0.59	0.08

Table 7 The electronic term (e_{iv}^e), nuclear term (e_{iv}^n), total direct 'proper' piezoelectric constant ($e_{iv} = e_{iv}^e + e_{iv}^n$) (all in C m^{-2} unit), and electro-mechanical (EM) coupling factor (k_{iv}) for X_2PbO_3 (X = K, Rb, Cs) using the PBE0 functional computed using the CPHF/KS analytical approach

	Electronic term					Nuclear term				
X	e_{31}^e	e_{32}^e	e_{33}^e	e_{24}^e	e_{15}^e	e_{31}^n	e_{32}^n	e_{33}^n	e_{24}^n	e_{15}^n
K	−0.02	0.10	−0.08	0.14	−0.05	0.36	−0.62	0.38	−0.43	0.34
Rb	0.02	−0.09	0.06	−0.11	0.05	−0.39	0.53	−0.34	0.31	−0.23
Cs	−0.01	0.03	−0.02	0.03	−0.02	0.28	−0.08	0.61	−0.03	0.00

	Total					EM coupling				
X	e_{31}	e_{32}	e_{33}	e_{24}	e_{15}	k_{31}	k_{32}	k_{33}	k_{24}	k_{15}
K	0.34	−0.52	0.30	−0.29	0.30	0.41	0.63	0.36	0.36	0.39
Rb	−0.37	0.44	−0.28	0.20	−0.19	0.44	0.52	0.33	0.24	0.23
Cs	0.27	−0.05	0.60	0.01	−0.02	0.31	0.06	0.69	0.01	0.02

3.6 Piezoelectric and electromechanical coupling properties

As a green method of energy conversion, piezoelectricity has attracted much attention among researchers. Piezoelectric materials may prove to be a viable and sustainable source of energy if an efficient device of high mechanical stress to atomic scale polarization can be discovered. As mentioned in Sections 1 and 3.2, due to the centrosymmetric nature of $C2/c$-X_2PbO_3 structures, the compounds LPO, and NPO do not possess piezoelectricity. Therefore, in this section, we will be focusing on the piezoelectric properties for the $Cmc2_1$-X_2PbO_3 materials, calculated based on PBE0 functionals, only $i.e.$, the most relevant functional in reproducing experimental lattice parameters for the investigated systems. In this work, piezoelectric tensors are computed using two different methodologies. Firstly, the direct and converse piezoelectric tensors are estimated through the numerical Berry phase (BP) approach which rely on the modern theory of polarization.[77] According to BP approach [see eqn (22)],

$$e_{iv} = \frac{|e|}{2\pi V}\sum_l a_{li}\frac{\delta\phi_l}{\delta\eta_v} \tag{22}$$

Here, e_{iv} is the direct piezoelectric tensor, e electron charge, V volume, a_{li} is the ith Cartesian component of the lth direct lattice basis vector a_l, ϕ_l is numerical first derivatives of the BP, and η_v the strain tensor. Also, $i = x, y, z$; $v = 1, 2, 3, 4, 5, 6$ ($1 = xx, 2 = yy, 3 = zz, 4 = yz, 5 = xz, 6 = xy$).

The direct and converse piezoelectric tensors are again related by the formula [see eqn (23)]:

$$\begin{aligned} e &= dC \\ d &= eS \end{aligned} \tag{23}$$

Secondly, the piezoelectric tensors are computed through an analytical approach based on the Coupled Perturbed Hartree–Fock/Kohn–Sham (CPHF/KS) scheme.[78,79] Herein, in addition to the electronic term's analytical computation, the internal-strain tensor is used to assess the nuclear-relaxation contribution instead of atomic coordinates' numerical geometry optimizations at strained configurations. The employed equation [see eqn (24)] for determining the nuclear-relaxation contribution is:

$$e_{iv}^n = \frac{-1}{V_0}\sum_{aj} Z_{i,aj}^* \Gamma_{aj,v} \tag{24}$$

Here, $\Gamma_{aj,v}$ and Z^* are the displacement-response internal-strain tensor which describes first order atomic displacements as induced by a first order strain, and the tensors containing the dynamic Born effective charges, respectively [see eqn (25)]:

$$\begin{aligned} Z_{i,aj}^* &= \left.\frac{\delta^2 E}{\delta\xi_i\delta u_{aj}}\right|_\eta \\ \Gamma_{aj,v} &= \left.\frac{-\delta u_{aj}}{\delta\eta_v}\right|_\xi \end{aligned} \tag{25}$$

where u_{aj} are Cartesian components of the displacement vector u_a of atom a ($j = x, y, z$).

The calculated piezoelectric tensors for $Cmc2_1$-X_2PbO_3 materials are presented in Table 6 for the BP numerical

approach and Table 7 for the CPHF/KS analytical approach. The direct ($e_{i\nu}$) and converse ($d_{i\nu}$) piezoelectricity presented in Table 6 determine the change of polarization under a finite strain and the strain induced by an applied electric field. At first glance, it can be noticed that from Table 6, the maximum direct piezoelectric constant from BP approach reduces as X goes from K $\rightarrow$ Cs (magnitude only). The increasing atomic masses of X-atoms when going from K $\rightarrow$ Cs progressively reduces the distortion of atomic positions from their equilibrium positions, resulting in the dis-amplification of polarization tensor which reduces the piezoelectric constants. For X = K and Rb the maximum responses are $e_{32} = -0.51$, and 0.45 C m^{-2} with the response direction along z-axis due to strain η_{yy}. Here, the negative sign (*i.e.*, for X = K) indicates a compressive strain that leads η_{yy} to a negative value. For X = Cs the maximum response is $e_{33} = 0.16$ C m^{-2}, which is in the z-axis direction and due to η_{zz} strain.

It is well-known that performing piezoelectric properties calculations in an analytical fashion using the internal-strain tensor of energy second-derivatives with respect to atomic displacements and lattice deformations in combination with the inter-atomic force constant Hessian matrix, *i.e.* CPHF/KS, approach shows better accuracy than performing the calculation through numerical geometry optimizations to relax atomic positions at actual strained lattice configurations, *i.e.* the BP approach. Therefore, more detailed calculations including the electronic ($e_{i\nu}^{e}$) and nuclear ($e_{i\nu}^{n}$) terms, and the total direct 'proper' ($e_{i\nu}$) piezoelectric constants through the CPHF/KS approach are reported in Table 7 for the $Cmc2_1$-X$_2$PbO$_3$ compounds. Evidently, each compound's total direct 'proper' piezoelectric response contribution from the $e_{i\nu}^{e}$ are negligibly small and also reduce as X moves from K $\rightarrow$ Cs. The degree of polarization reduced resulting from a decrease in electronegativity down the periodic table group, which suggests that the contribution of $e_{i\nu}^{e}$ has diminished. Consequently, $e_{i\nu}^{n}$ accounts for the majority of each material's total direct piezoelectric responses. Interestingly, the total direct and total direct 'proper' piezoelectric constants obtained from BP and CPHF/KS schemes agreed well for X = K, and Rb with deviations $|e_{i\nu}| <$ 0.02 C m^{-2}. However, in the case of X = Cs, a comparatively high piezoelectric constant appears for e_{31} and e_{33} when CPHF/KS is adopted. This discrepancy may arise from the inherently more robust nature of the CPHF/KS scheme in evaluating $e_{i\nu}^{n}$, as it explicitly accounts for the partitioning of the nuclear-relaxation contribution of the piezoelectric tensor into phonon-mode-resolved components, together with the enhanced ionic polarizability introduced by the larger Cs cation. In such cases, the Berry-phase formalism, which predominantly captures the macroscopic polarization response, tends to emphasize long-range ionic contributions, whereas the CPHF/KS approach, being more sensitive to local field effects, reflects short-range electronic–ionic interactions. Consequently, the disparity between the two methods becomes more pronounced in Cs$_2$PbO$_3$ than in its lighter alkali counterparts. Overall, the maximum piezoelectric constants attributed by each compound are higher than the α-quartz, a standard piezoelectric material, whose largest constant e_{11} is 0.15 C m^{-2} at room temperature and 0.07 C m^{-2} at 5 K.[80] Also, compared to the analogous

compounds such as Na$_2$SiO$_3$ and Na$_2$GeO$_3$, our results show better responses than for Na$_2$SiO$_3$ ($e_{32} = 0.22$ C m^{-2}), however they are lower than for Na$_2$GeO$_3$ ($e_{33} = 0.90$ C m^{-2}).[12,28]

The electromechanical (EM) coupling factors ($k_{i\nu}$) calculated using eqn (26) are presented in Table 7.[81] This determines the efficiency of a piezoelectric material *i.e.*, the factor with which the materials convert mechanical energy into electrical energy or *vice versa*.

$$k_{i\nu} = \frac{|e_{i\nu}|}{\sqrt{C_{44}\varepsilon_0\varepsilon_1(0)}} \tag{26}$$

Here, $e_{i\nu}$ are the piezoelectric constants, C_{44} is the elastic constant (in Pa unit), $\varepsilon_0 = 8.854 \times 10^{-12}$ F m^{-1} is the absolute permittivity of free space and $\varepsilon_1(0)$ is the real static dielectric constant.

Firstly, it can be noticed that the maximum $k_{i\nu}$ for each compound corresponds to the direction of their respective maximum piezoelectric constant. Even though the computed $k_{i\nu}$ shows its highest value for X = Cs with $k_{33} = 0.69$, the overall coupling factors when all the directions are taken into account is highest for X = K, with X = Rb serving as an intermediary. This reveals a better efficiency of the electromechanical transducer between the stated electric and elastic channels for X = K, and Rb. Since our results of the maximum $k_{i\nu}$ are higher than the quartz crystal[82] with a highest electromechanical coupling coefficient of ~0.29 in a direction which makes an angle of 73° with y axis in yz plane, the investigated $Cmc2_1$-X$_2$PbO$_3$ materials could be potential candidates which can serve as efficient piezoelectric materials.

3.7 Thermoelectric properties

The primary focus of this work is to identify the TE efficiency (ZT) of the investigated compounds, which is closely related to the electron transport properties such as Seebeck coefficient (S), electrical conductivity (σ), electron thermal conductivity (κ_e), and the lattice thermal conductivity (κ_L). For this particular calculation, we have considered not only the p-type and n-type doping, but also the TE properties along the x, y, and z-axes by employing four different functionals such as PBE-GGA, B3LYP, HSE06, and PBE0. Herein, calculations for the electron transport properties are performed using the Boltzmann transport equation (BTE) within the CRTA at fixed $\tau = 10$ fs (10^{-14} s) using BoltzTraP.[7] The employed formulae for thermoelectric parameter calculations are:[83,84]

$$\sigma(\mu, T) = e^2 \int dE \left(\frac{-\delta f_0}{\delta E}\right) \Xi_{qr}(E) \tag{27}$$

$$S(\mu, T) = \frac{e}{T} \int dE \left(\frac{-\delta f_0}{\delta E}\right)(E - \mu) \Xi_{qr}(E) \tag{28}$$

$$\kappa_e(\mu, T) = \frac{1}{T} \int dE \left(\frac{-\delta f_0}{\delta E}\right)(E - \mu)^2 \Xi_{qr}(E) \tag{29}$$

where, μ is the chemical potential or the Fermi level, E is the energy, f_0 is the Fermi–Dirac distribution and Ξ is the kernel of the transport distribution function (TDF). Here, Ξ is further expressed as:

$$\Xi_{qr}(E) = \tau \sum_k \frac{1}{N_k} \frac{1}{V} \sum_{i,j} v_{i,q}(k)v_{j,r}(k)\delta(E - E_i(k)) \quad (30)$$

where, $v_{i,q}(k)$ is the velocity of the ith band calculated along the Cartesian direction q, τ is the lifetime which is assumed to be constant according to the RTA. In the above equations, σ is the electrical conductivity, S is the Seebeck coefficient, and κ_e is the electronic thermal conductivity.

Here, the purpose for calculating the electronic transport properties is to obtain TE efficiency (figure of merit) ZT, given by

$$ZT = \frac{S^2 \sigma T}{\kappa_T} \quad (31)$$

where, κ_T is the total thermal conductivity and is equal to $\kappa_e + \kappa_L$. To determine the lattice contribution to the thermal conductivity (κ_L), we employed the well-known Slack equation given by[85]

$$\kappa_L = \frac{A\overline{M}\Theta_D^{3}\delta}{\gamma^2 Tn^{\frac{2}{3}}} \quad (32)$$

where, a constant $A = \dfrac{2.43 \times 10^{-8}}{1 - 0.514/\gamma + 0.228/\gamma^2}$, $\overline{M}$ is average atomic mass, Θ_D is the Debye temperature, δ^3 is the volume per atom, γ is the Gruneisen parameter, and n is the number of atoms per unit cell.

From the transport properties of electrons with respect to chemical potential (μ) presented in Fig. S2–S14, considering the direction-wise analysis, one can find that each of the transport properties for the investigated materials are highly anisotropic in nature with the z-axis the most preferable direction for achieving maximum TE efficiency except for in LPO where it is obtained along x-axis. Also, from these plots, it can be deduced that all of the compounds under investigation exhibit a p-type semi-conducting nature, with holes serving as the majority of carriers, regardless of the functionals employed. With hybrid functionals, each compound's E_g increases which in turn raises the $(E - \mu)$ term of eqn (28). This subsequently maximizes the Seebeck coefficient (S) computed using hybrid-DFT when compared to the PBE-GGA results [see Fig. S9–S11]. Also, on analyzing and comparing the PBE-GGA and hybrid-DFT band structure profiles of the investigated compounds [see Fig. 5 and S1], it is evident that the incorporated hybrid functionals have had a notable impact, particularly with regard to the energy levels where the electronic band lines are positioned. Thus, these substantial variations in band profiles due to the functionals employed has led to considerable changes in the ensuing transport properties. The resultant change in band energy due to the different functionals being adopted has led to the change in density of states, being a key factor for which the term $-\delta f_0/\delta E$ of eqn (27)–(29), that defines the number of states mapped and offered information of the channel allowing the charges to flow, varies. This phenomenon leads to remarkable changes of each compound's electrical conductivity (σ) and electron thermal conductivity (κ_e), when the PBE-GGA and hybrid-DFT computed transport properties are compared.

The primary aim for calculating transport properties is to obtain the figure of merit (ZT) which determines the material's

TE efficiency. In this regard, the TE power factor (PF = $S^2\sigma$) is firstly computed that measures the TE performance of the materials. The PFs with respect to chemical potential plots are depicted in Fig. S12–S14. From these plots, it is revealed that the PF increased as temperature rises, suggesting the enhancement of TE efficiency of the materials with temperature. It is important to note that the first peak points of PF along the left and right sides of the zero chemical potential (Fermi energy) corresponds to the optimum chemical potentials for p-type and n-type doping at various temperatures, where the optimal ZT values are determined as a function of temperature. Obviously, the ZT [see eqn (31)] depends on the conflicting nature of σ and κ_e, S and also on the κ_L. Since, the transport properties from BoltzTraP does not generate κ_L, therefore an analytical Slack model given in eqn (32) is employed which shows reliable κ_L values for complex materials compared to κ_L estimated from the phonon BTE calculations.[86] The obtained κ_L curves in Fig. 9 show continuously decreasing plots as the temperature rises due to the increasing phonon scattering. The larger atomic sizes as X goes from K → Cs for $Cmc2_1$-X_2PbO_3 materials result in a reduced possibility of phonon scattering down the group. Thus, the order of κ_L for $Cmc2_1$-X_2PbO_3 materials is KPO > RPO > CPO. However, our observation shows a conflicting nature for $C2/c$-X_2PbO_3 compounds where κ_L of NPO > κ_L of LPO. This might be due to the LPO attaining a higher density than NPO, which decreases heat transfer average distances, and therefore minimizes κ_L for LPO. Furthermore, the non-centrosymmetric distortions in the $Cmc2_1$-X_2PbO_3 phase contribute to enhanced phonon scattering, leading to lower κ_L values and improved thermoelectric performance relative to the centro-symmetric $C2/c$-X_2PbO_3 counterparts. Additionally, the calculated κ_L values for $Cmc2_1$-X_2PbO_3 compounds are lower than those of the structurally related $Cmc2_1$-Li_2GeO_3 compounds, which can be attributed to the presence of the heavy Pb atom.[87] The increased atomic mass of Pb further suppresses phonon transport, reinforcing the observed reduction in κ_L. Evidently,
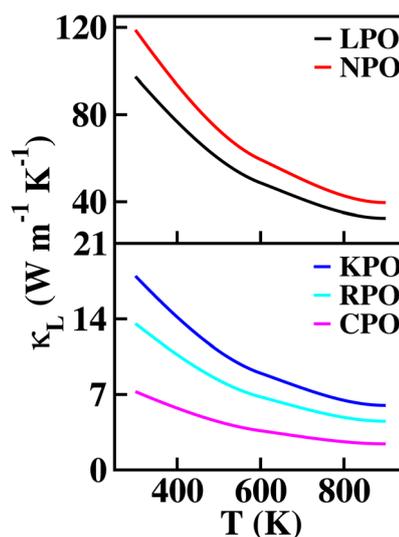

Fig. 9 Calculated lattice thermal conductivity (κ_L) of X_2PbO_3 compounds using the Slack equation.
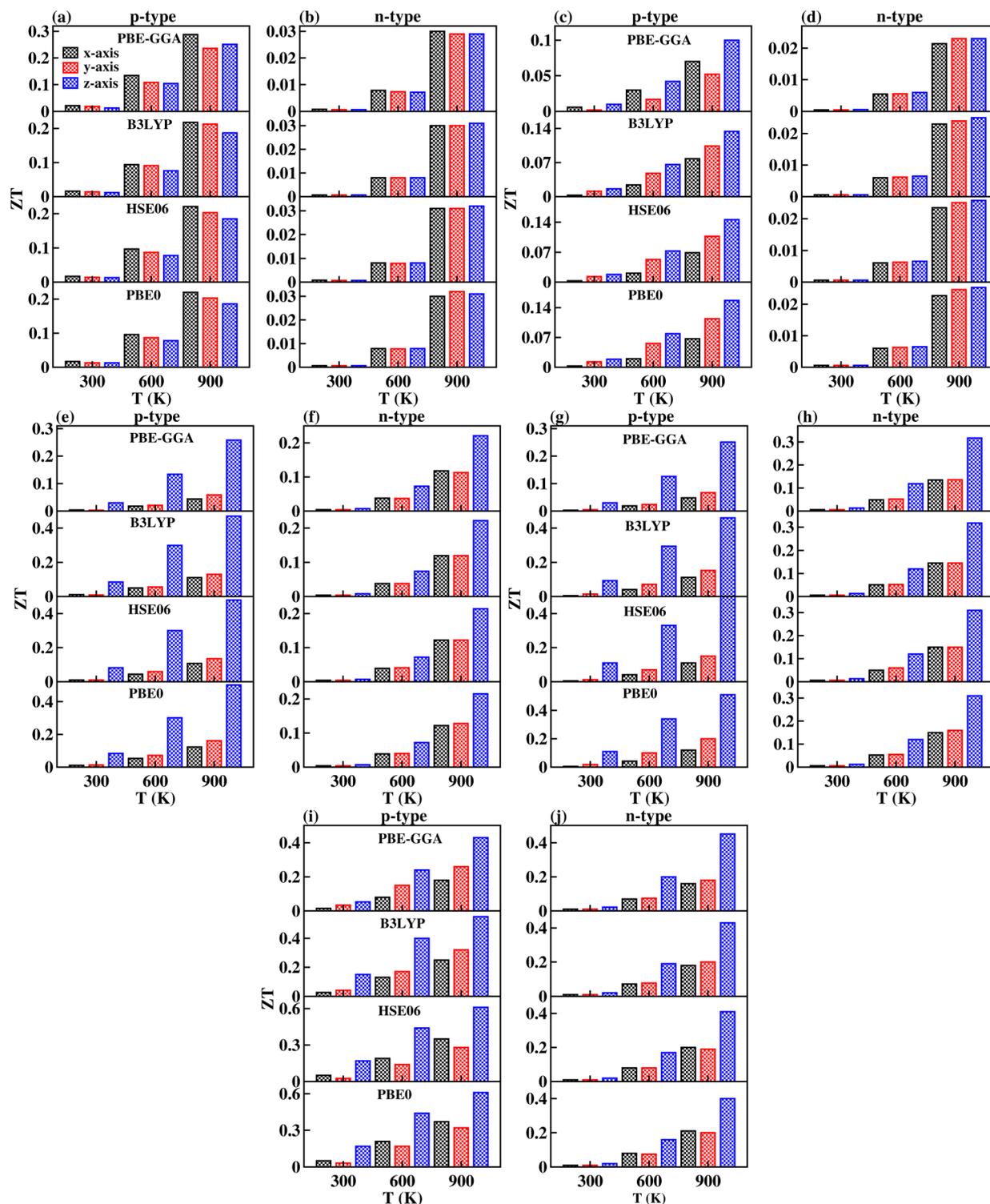
Fig. 10 Calculated thermoelectric efficiency (ZT) as a function of temperature using PBE-GGA, B3LYP, HSE06, and PBE0 functionals: (a) p-type and (b) n-type for Li_2PbO_3, (c) p-type and (d) n-type for Na_2PbO_3, (e) p-type and (f) n-type for K_2PbO_3, (g) p-type and (h) n-type for Rb_2PbO_3, and (i) p-type and (j) n-type for Cs_2PbO_3.

from the ZT plot as a function of temperature shown in Fig. 10, it can be seen that each compound's ZT value improves as the temperature increases. Furthermore, it can be determined that CPO has attained the best TE efficiency with $ZT = 0.61$ at $T =$

900 K along the z-direction for p-type doping with the PBE0 functional. Interestingly, each material's computed ZT from hybrid-DFT shows better efficiency when compared to the PBE-GGA result, except for LPO where the PBE-GGA estimates the

greatest ZT values. The present findings are noteworthy, even though the achieved TE efficiency remains moderate (given that the benchmark for high-performance thermoelectric materials is $ZT \geq 1$). This study represents the first theoretical report on the TE properties of $C2/c$-X_2PbO_3 and $Cmc2_1$-X_2PbO_3 glass-like compounds, which exhibit appreciable ZT values at elevated temperatures. Nevertheless, further in-depth investigations are required to enhance the electrical conductivity, particularly for the $Cmc2_1$-X_2PbO_3 phase, to realize their potential applicability in future thermoelectric devices. In general, glass-like materials crystallizing in the orthorhombic $Cmc2_1$ phase are known to possess relatively low electrical conductivity, which intrinsically restricts their TE efficiency. Consequently, only limited studies have explored this class of compounds. Reported data indicate that pristine glass-like Li_2GeO_3 displays a maximum ZT of merely 0.35 at 1200 K, which is significantly lower than the values obtained in the present work, underscoring the comparative promise of the investigated systems.[87] This finding suggests that, within the family of glass-like materials, X_2PbO_3 holds considerable promise as a next-generation thermoelectric candidate.

4 Conclusion

We present a comprehensive investigation of the multifunctional properties of X_2PbO_3 (X = Li, Na, K, Rb, and Cs) using hybrid-DFT within the frameworks of B3LYP, HSE06, and PBE0 functionals. Our study reveals that X_2PbO_3 compounds crystallize in two distinct structural phases, namely the monoclinic ($C2/c$) and orthorhombic ($Cmc2_1$) symmetries, depending on the ionic radius of the X-site atoms. To ensure the practical feasibility of these materials, we conducted a series of stability assessments: (1) the room temperature stability (from MD-simulation), (2) mechanical stability confirmed using Born's criteria, and (3) ground-state stability or energetic stability established from formation energy calculations. The electronic band structure analysis demonstrates a significant band gap increasing within the hybrid functionals, highlighting the semiconducting nature of X_2PbO_3. From the optical property calculations, we observed a strong absorption coefficient ($\alpha > 1 \times 10^5$ cm^{-1}) within the ultraviolet (UV) region, suggesting their potential use as UV-radiation shielding materials. The piezoelectric properties of the $Cmc2_1$-X_2PbO_3 phase were evaluated using both the PB and CPHF/KS formalism. The calculated piezoelectric coefficients are comparable to those of benchmark piezoelectric materials such as α-quartz (α-SiO_2), underscoring the promising electromechanical potential of X_2PbO_3. Nevertheless, the effective macroscopic performance in practical devices will depend on factors including crystallographic orientation, poling conditions, and domain engineering, which can modulate the intrinsic response predicted here. Complementary thermoelectric analyses further reveal that these compounds exhibit favorable high-temperature transport characteristics, indicating their suitability for waste-heat recovery and energy-conversion applications. Overall, this work demonstrates the multifunctional potential of X_2PbO_3 for piezoelectric, thermoelectric, and optoelectronic applications.

Experimental validation is encouraged to substantiate the predicted responses. Moreover, the present findings offer valuable guidance for computational researchers in selecting hybrid functionals optimized for reproducing structural parameters in DFT-based studies. Future efforts incorporating intrinsic defects, vacancies, or intentional doping are expected to enhance the thermoelectric performance and advance these materials toward practical device-level implementation.

Author contributions

R. Zosiamliana: performed detail calculations, formal analysis, visualization, validation, literature review, writing – original draft, writing – review & editing. Lalhriat Zuala: formal analysis, visualization, validation, writing – review & editing. Lalrinthara Pachuau: formal analysis, visualization, validation, writing – review & editing. Lalmuanpuia Vanchhawng: formal analysis, visualization, validation, writing – review & editing. S. Gurung: formal analysis, visualization, validation, writing – review & editing. A. Laref: formal analysis, visualisation, validation, writing – review & editing. Shalika Ram Bhandari: formal analysis, visualisation, validation, writing – review & editing. D. P. Rai: project management, supervision, resources, software, formal analysis, visualisation, validation, writing – review & editing.

Conflicts of interest

The authors declare no competing financial interest

Data availability

All data supporting the findings of this study are available within the article and its supplementary information (SI). Additional datasets generated and/or analysed during the current study are available from the corresponding author on reasonable request.

Supplementary information is available. See DOI: https://doi.org/10.1039/d5ra07886e.

Acknowledgements

References

1 R. Martins, *Prog. Nat. Sci. Mater. Int.*, 2021, **31**, 785–791.
2 T. M. Tritt and M. A. Subramanian, *MRS Bull.*, 2006, **31**, 188–198.
3 R. Freer and A. V. Powell, *J. Mater. Chem. C*, 2020, **8**, 441–463.
4 Z. Soleimani, S. Zoras, B. Ceranic, S. Shahzad and Y. Cui, *Sustain. Energy Technol. Assessments*, 2020, **37**, 100604.

5 P. A. Finn, C. Asker, K. Wan, E. Bilotti, O. Fenwick and C. B. Nielsen, *Front. Electron. Mater.*, 2021, **1**, 677845.

6 R. Singh, S. Dogra, S. Dixit, N. I. Vatin, R. Bhardwaj, A. K. Sundramoorthy, H. Perera, S. P. Patole, R. K. Mishra and S. Arya, *Hybrid Adv.*, 2024, **5**, 100176.

7 G. K. Madsen and D. J. Singh, *Comput. Phys. Commun.*, 2006, **175**, 67–71.

8 R. Holomb, V. Mitsa, S. Akyuz and E. Akalin, *Philos. Mag.*, 2013, **93**, 2549–2562.

9 H. Gong, B. Song, Y. Yang, P. Wang, Z. Cao, X. Chen, G. Zhao, S. Peng, Y. Liu and G. Han, *J. Am. Ceram. Soc.*, 2021, **104**, 3198–3211.

10 Z. E. Biskri, H. Rached, M. Bouchear and D. Rached, *J. Mech. Behav. Biomed. Mater.*, 2014, **32**, 345–350.

11 J. Du and L. R. Corrales, *J. Chem. Phys.*, 2006, **125**, 114702.

12 Z. Renthlei, M. Prasad, J. Sivakumar, L. Zuala, L. Pachuau, Y. R. Devi, N. S. Singh, G. Abdurakhmanov, A. Laref and D. P. Rai, *ACS Omega*, 2023, **8**, 16869–16882.

13 R. Hoppe, H.-J. Rohrborn and H. Walker, *Naturwissenschaften*, 1964, **51**, 86.

14 P. Panek and R. Hoppe, *Z. Anorg. Allg. Chem.*, 1972, **393**, 13–22.

15 R. Hoppe and H. Stöver, *Z. Anorg. Allg. Chem.*, 1977, **437**, 123–126.

16 B. Brazel and R. Hoppe, *Z. Naturforsch., B: J. Chem. Sci.*, 1982, **37**, 1369–1374.

17 W. H. Zachariasen, *J. Am. Chem. Soc.*, 1932, **54**, 3841–3851.

18 O. Mezilet, A. Assali, S. Meskine, A. Boukortt and M. Halati, *Mater. Today Commun.*, 2022, **31**, 103371.

19 O. Sadouki, F. Khelfaoui, F. Fontaine-Vive, K. Boudia, H. Hocine, E. Sert, A. R. Benrekia, M. Hamlat, A. Slamani, F. Belkharroubi and K. Amara, *J. Electron. Mater.*, 2023, **52**, 6778–6790.

20 Y. Zhang, W. Qu, G. Peng, C. Zhang, Z. Liu, J. Liu, S. Li, H. Wu, L. Meng and L. Gao, *Materials*, 2022, **15**, 487.

21 C. A. McKay, *J. Med. Toxicol.*, 2013, **9**, 339–343.

22 G. Flora, D. Gupta and A. Tiwari, *Biol. Trace Elem. Res.*, 2013, **152**, 31–40.

23 C. Yedjou and P. Tchounwou, *Int. Res. J. Publ. Environ. Health*, 2007, **4**, 132–137.

24 F. Frongia, M. Pilloni, A. Scano, A. Ardu, C. Cannas, A. Musinu, G. Borzone, S. Delsante, R. Novakovic and G. Ennas, *J. Alloys Compd.*, 2015, **623**, 7–14.

25 A. B. F. Vitoreti, S. Agouram, M. Solis de la Fuente, V. Muñoz-Sanjosé, M. A. Schiavon and I. Mora-Seró, *J. Phys. Chem. C*, 2018, **122**, 14222–14231.

26 Z. Renthlei, L. Celestine, L. Kima, L. Zuala, Z. Mawia, B. Chettri, Y. T. Singh, S. Abdullaev, M. Ezzeldien and D. P. Rai, *Energy Fuels*, 2023, **37**, 19831–19844.

27 R. Zosiamliana, Lalrinkima, B. Chettri, G. Abdurakhmanov, M. P. Ghimire and D. P. Rai, *RSC Adv.*, 2022, **12**, 12453–12462.

28 R. Zosiamliana, B. Chettri, G. S. L. Fabris, J. R. Sambrano, S. Abdullaev, G. Abdurakhmanov and D. P. Rai, *RSC Adv.*, 2022, **12**, 27666–27678.

29 M. Chira, A. Hegyi, H. Szilagyi and H. Vermeșan, *The 14th International Conference on Interdisciplinarity in Engineering—INTER-ENG 2020*, Basel Switzerland, 2020, p. 35.

30 S. Gelin, N. E. Kirchner-Hall, R. R. Katzbaer, M. J. Theibault, Y. Xiong, W. Zhao, M. M. Khan, E. Andrewlavage, P. Orbe, S. M. Baksa, M. Cococcioni, I. Timrov, Q. Campbell, H. Abruña, R. E. Schaak and I. Dabo, *PRX Energy*, 2024, **3**, 013007.

31 R. Dovesi, A. Erba, R. Orlando, C. M. Zicovich-Wilson, B. Civalleri, L. Maschio, M. Rérat, S. Casassa, J. Baima, S. Salustro and B. Kirtman, *Wiley Interdiscip. Rev.: Comput. Mol. Sci.*, 2018, **8**, e1360.

32 D. Vilela Oliveira, J. Laun, M. F. Peintinger and T. Bredow, *J. Comput. Chem.*, 2019, **40**, 2364–2376.

33 J. Laun and T. Bredow, *J. Comput. Chem.*, 2022, **43**, 839–846.

34 J. P. Perdew, K. Burke and M. Ernzerhof, *Phys. Rev. Lett.*, 1996, **77**, 3865–3868.

35 A. D. Becke, *Phys. Rev. A: At., Mol., Opt. Phys.*, 1988, **38**, 3098–3100.

36 C. Lee, W. Yang and R. G. Parr, *Phys. Rev. B: Condens. Matter Mater. Phys.*, 1988, **37**, 785–789.

37 C. Adamo and V. Barone, *J. Chem. Phys.*, 1999, **110**, 6158–6170.

38 J. Heyd, G. E. Scuseria and M. Ernzerhof, *J. Chem. Phys.*, 2003, **118**, 8207–8215.

39 M. Y. Mehboob, R. Hussain, M. Adnan, Saira, U. Farwa, Z. Irshad and M. R. Saeed Ashraf Janjua, *J. Phys. Chem. Solids*, 2022, **162**, 110508.

40 J. D. Head and M. C. Zerner, *Chem. Phys. Lett.*, 1985, **122**, 264–270.

41 N. Nawi, M. Ransing and R. Ransing, *Sixth International Conference on Intelligent Systems Design and Applications*, 2006, pp. 152–157.

42 H. J. Monkhorst and J. D. Pack, *Phys. Rev. B*, 1976, **13**, 5188–5192.

43 S. Nosé, *Mol. Phys.*, 2002, **100**, 191–198.

44 H. C. Andersen, *J. Chem. Phys.*, 1980, **72**, 2384–2393.

45 S. Smidstrup, T. Markussen, P. Vancraeyveld, J. Wellendorff, J. Schneider, T. Gunst, B. Verstichel, D. Stradi, P. A. Khomyakov, U. G. Vej-Hansen, M.-E. Lee, S. T. Chill, F. Rasmussen, G. Penazzi, F. Corsetti, A. Ojanperä, K. Jensen, M. L. N. Palsgaard, U. Martinez, A. Blom, M. Brandbyge and K. Stokbro, *J. Phys.: Condens. Matter*, 2020, **32**, 015901.

46 T. J. Scheidemantel, C. Ambrosch-Draxl, T. Thonhauser, J. V. Badding and J. O. Sofo, *Phys. Rev. B: Condens. Matter Mater. Phys.*, 2003, **68**, 125210.

47 B. Ryu and M.-W. Oh, *J. Korean Ceram. Soc.*, 2016, **53**, 273–281.

48 K. Momma and F. Izumi, *J. Appl. Crystallogr.*, 2008, **41**, 653–658.

49 F. Birch, *Phys. Rev.*, 1947, **71**, 809–824.

50 F. D. Murnaghan, *Am. J. Math.*, 1937, **59**, 235.

51 M. Parrinello and A. Rahman, *J. Appl. Phys.*, 1981, **52**, 7182–7190.

52 M. Parrinello and A. Rahman, *Phys. Rev. Lett.*, 1980, **45**, 1196–1199.

53 S. Nose, *J. Phys.: Condens. Matter*, 1990, **2**, SA115–SA119.

54 R. S. Mulliken, *J. Chem. Phys.*, 1955, **23**, 1833–1840.

55 N. T. Han, V. K. Dien, N. T. Thuy Tran, D. K. Nguyen, W.-P. Su and M.-F. Lin, *RSC Adv.*, 2020, **10**, 24721–24729.

56 V. K. Dien, H. D. Pham, N. T. T. Tran, N. T. Han, T. M. D. Huynh, T. D. H. Nguyen and M. Fa-Lin, *Sci. Rep.*, 2021, **11**, 4939.

57 U. V. Waghmare and K. M. Rabe, *Phys. Rev. B: Condens. Matter Mater. Phys.*, 1997, **55**, 6161–6173.

58 Y. Mo, S. P. Ong and G. Ceder, *Phys. Rev. B: Condens. Matter Mater. Phys.*, 2011, **84**, 205446.

59 C. Ambrosch-Draxl and J. O. Sofo, *Comput. Phys. Commun.*, 2006, **175**, 1–14.

60 M. Born, *Math. Proc. Camb. Phil. Soc.*, 1940, **36**, 160–172.

61 F. Mouhat and F.-X. Coudert, *Phys. Rev. B: Condens. Matter Mater. Phys.*, 2014, **90**, 224104.

62 W. Voigt, *Lehrbuch der Kristallphysik*, Vieweg + Teubner Verlag, Wiesbaden, 1966.

63 A. Reuss, *J. Appl. Math. Mech.*, 1929, **9**, 49–58.

64 R. Hill, *Proc. Phys. Soc., London, Sect. A*, 1952, **65**, 349–354.

65 L. Kleinman, *Phys. Rev.*, 1962, **128**, 2614–2621.

66 D. H. Chung and W. R. Buessem, *J. Appl. Phys.*, 1968, **39**, 2777–2782.

67 D. G. Cahill and R. Pohl, *Solid State Commun.*, 1989, **70**, 927–930.

68 J.-i. Tani, M. Takahashi and H. Kido, *Phys. B*, 2010, **405**, 4219–4225.

69 H. Chen and L. Yang, *Phys. B*, 2011, **406**, 4489–4493.

70 Lalrinkima, C. E. Ekuma, T. C. Chibueze, L. A. Fomin, I. V. Malikov, L. Zadeng and D. P. Rai, *Phys. Chem. Chem. Phys.*, 2021, **23**, 11876–11885.

71 S. Baroni, P. Giannozzi and E. Isaev, *Rev. Mineral. Geochem.*, 2010, **71**, 39–57.

72 M. Blanco, E. Francisco and V. Luaña, *Comput. Phys. Commun.*, 2004, **158**, 57–72.

73 M. Palumbo and A. Dal Corso, *J. Phys.: Condens. Matter*, 2017, **29**, 395401.

74 M. Palumbo and A. Dal Corso, *Phys. Status Solidi B*, 2017, **254**, 1700101.

75 A. C. Holt and M. Ross, *Phys. Rev. B*, 1970, **1**, 2700–2705.

76 D. Belmonte, C. Gatti, G. Ottonello, P. Richet and M. Vetuschi Zuccolini, *J. Phys. Chem. A.*, 2016, **120**, 8881–8895.

77 A. Erba, K. E. El-Kelany, M. Ferrero, I. Baraille and M. Rérat, *Phys. Rev. B: Condens. Matter Mater. Phys.*, 2013, **88**, 035102.

78 J. Baima, A. Erba, L. Maschio, C. M. Zicovich-Wilson, R. Dovesi and B. Kirtman, *Z. Phys. Chem.*, 2016, **230**, 719–736.

79 A. Erba, *Phys. Chem. Chem. Phys.*, 2016, **18**, 13984–13992.

80 R. Tarumi, K. Nakamura, H. Ogi and M. Hirao, *J. Appl. Phys.*, 2007, **102**, 113508.

81 L. Celestine, R. Zosiamliana, L. Kima, B. Chettri, Y. T. Singh, S. Gururng, N. S. Singh, A. Laref and D. P. Rai, *J. Phys.: Condens. Matter*, 2024, **36**, 325501.

82 K. Yu and T. Liu, *Optoelectronic Devices and Integration III*, 2010, p. 78471K.

83 J. Linnera, G. Sansone, L. Maschio and A. J. Karttunen, *J. Phys. Chem. C*, 2018, **122**, 15180–15189.

84 G. Sansone, A. Ferretti and L. Maschio, *J. Chem. Phys.*, 2017, **147**, 114101.

85 G. A. Slack, *Solid State Physics - Advances in Research and Applications*, 1979, vol. 34, pp. 1–71.

86 P. Joshi, G. B. Acharya, I. B. Khadka, B. Srinivasan, S.-H. Kim and M. P. Ghimire, *ACS Appl. Energy Mater.*, 2025, **8**, 3217–3228.

87 R. Zosiamliana, L. Celestine, L. Zuala, B. Chettri, Z. Mawia, G. Abdurakhmanov, A. Laref, S. R. Bhandari and D. P. Rai, *High Press. Res.*, 2024, 1–28.